Shap. Mem. Superelasticity (2018) 4:327–336
https://doi.org/10.1007/s40830-018-0176-x

# Powder Metallurgy Fabrication of Porous 51(at.%)Ni–Ti Shape Memory Alloys for Biomedical Applications

**Mustafa K. Ibrahim[1] · E. Hamzah[1] · Safaa N. Saud[2] · E. M. Nazim[1]**

Published online: 21 May 2018


**Abstract** The effect of time and temperature on the microwave sintering of 51(at.%)Ni–Ti shape memory alloys (SMAs) was investigated in the current research. Furthermore, the microstructure, mechanical properties, and bio-corrosion properties were analyzed based on the sintering conditions. The results revealed that the sintering condition of 700 °C for 15 min produced a part with coherent surface survey that does not exhibit gross defects. Increasing the sintering time and temperature created defects on the outer surface, while reducing the temperature to 550 °C severely affected the mechanical properties. The microstructure of these samples showed two regions of Ni-rich region and Ti-rich region between them $Ti_2Ni$, NiTi, and $Ni_3Ti$ phases. The differential scanning calorimeter (DSC) curves of Ni–Ti samples exhibited a multi-step phase transformation B19′–R–B2 during heating and cooling. An increase in the sintering temperature from 550 to 700 °C was found to increase the fracture strength significantly and decreased the fracture strain slightly. Reducing the sintering temperature from 700 to 550 °C severely affected the corrosion behaviors of 51%Ni–Ti SMAs. This research aims to select the optimum parameters to produce Ni–Ti alloys with desired microstructure, mechanical properties, and corrosion behaviors for biomedical applications.

✉ E. Hamzah
mustafakhaleel4@gmail.com

[1] Faculty of Mechanical Engineering, Universiti Teknologi Malaysia, 81310 UTM Johor Bahru, Johor, Malaysia

[2] Faculty of Information Sciences and Engineering, Management & Science University, Shah Alam, Selangor, Malaysia

**Keywords** Porous 51%Ni–Ti SMAs · Microwave sintering · Microstructure · Mechanical properties and corrosion · Bioactivity

## Introduction

Shape memory alloys (SMAs) provide a unique combination of several important properties, including the shape memory effect (SME), superelasticity (SE) or pseudoelasticity (PE) and high damping capacity [1]. Titanium-based alloys have been widely used as implants as dental, knee, and hip implants because of their ductility, corrosion resistance, and high yield strength [2, 3]. Similarly, NiTi alloys exhibit corrosion resistance and biocompatibility based on historical in vitro *and* in vivo studies [4–7], mainly from the formation of a passive dense titanium-oxide layer ($TiO_2$). Porous Ni–Ti alloys have attracted interest for bio implantation due to the presence of the pores in the bulk material which can elicit in-growth of body tissue, decrease density of the alloy and improve fixation [8]. Therefore, alternative processes such as mechanical alloying (MA) and powder metallurgy (PM) fabrication processes can be utilized to control grain sizes and compositions [9, 10]. PM is a promising method for producing of porous near-net-shape components [11, 12]. There are six PM methods to fabricate dense or porous Ni–Ti alloys from elemental and/or pre-alloyed powders; these methods are spark plasma sintering (SPS) [11], hot isostatic pressing (HIP) for sintering materials at elevated pressure [13], cold pressing and sintering or conventional sintering (CS) [14], self-propagating high-temperature synthesis (SHS) [15, 16], metal injection molding (MIM) [17, 18], and microwave sintering (MWS) [19, 20]. Microwave sintering is a relatively new method to prepare Ni–Ti

alloys. It is a new sintering method for metals, composites, ceramics, and semiconductors [21–23]. The advantages of microwave sintering are reducing the time and the energy of the process, enhancing the diffusion, providing rapid heating rates, and improving mechanical and physical properties [21, 22]. The presence of pores reduces the elastic modulus [19, 24, 25] and creates a platform for the host tissue cells to attach and grow into the pores, resulting in an integration with the host tissue cells [25–27]. Reducing the elastic modulus reduces the effect of "stress shielding" generated due to a large mismatch of elastic modulus between a solid metal implant (e.g., Ti-alloys) materials (> 100 GPa) and hard tissue (< 20 GPa). "Stress shielding" causes the resorption of the surrounding hard tissue, loosening of the implants which may lead to an implant failure [28–30]. Several researchers used the space-holder method to produce porous Ti-based alloys [31–35] and foam structures of different metal powders [36–38]. One of the problems of using the space holder technique is the added steps to remove the space holder material from the green compact during the sintering process [39]. The conventional sintering process is vulnerable to contamination from the spacer-holder material residue and other process-related contaminants. Contamination may occur due to the presence of oxygen, nitrogen dissolved in titanium or titanium alloys via increasing temperature during the sintering process; such contaminates can adversely impact the mechanical properties [33].

## Experimental Procedure

### Sample Preparation

In this work, the elemental powders of Ti and Ni were prepared via a PM process. The specification of the elemental powder, composition, and ball milling parameters are shown in Table 1. These powders of 51(at.%)Ni–Ti SMAs were prepared by MA using a planetary ball mill (PM100). The mixed powders were then cold-pressed to green samples of Φ25 × 10 mm under a uniaxial pressure of 230 kg/cm$^2$ for 5 min, followed by microwave sintering (HAMiLab-V3, SYNOTHERM Corp.). The green 51%Ni–Ti samples were microwave sintered at 550 and 700 °C for 15 min, 800 and 1200 °C for 5 min, and 800 and 900 °C for 30 min at a heating rate of 30 °C/min. Figure 1 is a schematic diagram of the MWS vacuum pot containing the insulation barrel that was set up continuously at 2.45 GHz and 4.5 kV. Microwave sintering was performed under a flow of high-purity Ar gas. The green samples were placed in an alumina crucible surrounded by silicon carbide (SiC) particles. An infrared pyrometer was used to measure the temperature of the samples during sintering.

The sintered samples were electrical discharge machined (EDM) into 7 mm × 7 mm × 14 mm dimensions for compression testing based on ASTM E9-09 and dimensions of 10 mm × 10 mm × 20 mm for shape memory testing. The corrosion test was performed with Φ13.5 × 2 mm samples.

### Microstructural Characterization

Several techniques were used to analyze and characterize the Ni–Ti SMAs, such as scanning electron microscopy (SEM), X-ray diffraction (XRD), differential scanning calorimetry (DSC), and energy-dispersive X-ray spectroscopy (EDAX). A Nikon optical microscopy was used to analyze the as-polished surfaces to identify the pores size, pores shape, and pores distribution of Ti-Ni samples assisted by Isolution Lite" software. The surface was then etched in a 10%HF–40%$HNO_3$–50% distilled water solution and examined by scanning electron microscopy (SEM, Hitachi Model S-3400 N). An Archimedes drainage method was used to determine the porosity of the samples. The X-ray diffractometer (XRD, D5000 Siemens) was used to characterize the phase composition of 51%Ni–Ti SMAs; the planes of the phase composition were identified by a Jade software. The X-ray diffractometer fitted with a Cu Kα X-ray source and the scanning mode was locked couple, with a scan rate of 0.05°/s, and 2$\theta$ range between 20 and 90 °C. Differential scanning calorimeter (DSC Q200, TA Instrument) was used to identify the phase transformation temperatures of these alloys using TA Instrument software under heating/cooling rates of 10 °C/min.

**Table 1** Specification of elemental powders and mixtures

| Element | Powder specification | | | Ball milling parameters | | |
|---|---|---|---|---|---|---|
| | Purity (%) | Size (μm) | Composition (at.%) | Rotation speed (rpm) | Bal-to-powder ratio | Time (h) |
| Ti | 99.5 | 150 | 49 | 300 | 4:1 | 1 |
| Ni | 99.5 | 45 | 51 | | | |

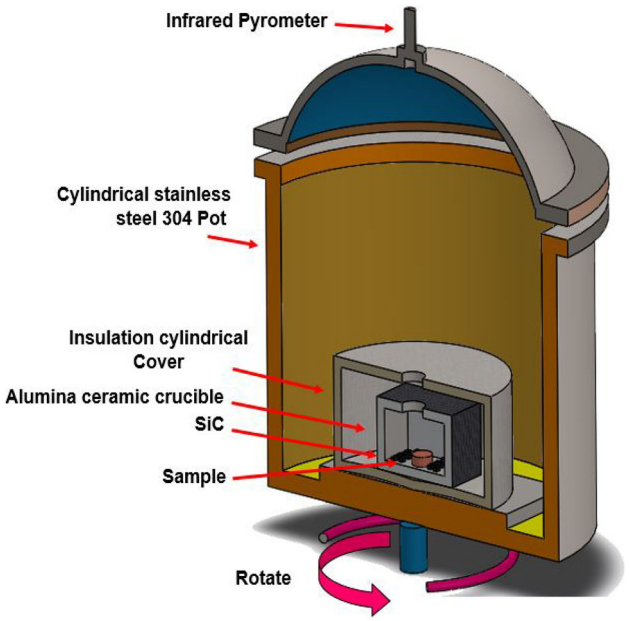


**Fig. 1** Schematic diagram of MWS vacuum pot containing the insulation barrel

### Mechanical Tests

An Instron 600 DX-type universal testing machine was used to perform the compression test at a constant speed of 0.5 mm/min at 27 °C.

### Electrochemical Test

The corrosion resistance was measured using a potentiodynamic polarization (PDP) test in a simulated body fluid (SBF). The test samples were connected to an open-air glass cell with a surface area of 0.2 $cm^2$. The open-air glass cell contained around 300 mL SBF of pH 7.4 at, 37 °C. The scan rate was set to 2 mV/s, and the test was started at − 250 mV. A VersaSTAT 3 machine (Princeton Applied Research) was used to record-data from the three-electrode cells attached to the equipment; (1) a saturated calomel electrode (SCE) reference electrode, (2) a graphite rod was a counter electrode, and (3) a working electrode (the test part). Each electrochemical test was rerun three times for each sample to ensure the reproducibility of the results. The corrosion rate ($R_i$) and the polarization resistance ($R_p$) of these samples were calculated according to [40, 41]

$$R_i = 22.85 i_{corr} \quad (1)$$

$$R_p = \frac{\beta_a \beta_c}{2.3(\beta_a + \beta_c) i_{corr}}, \quad (2)$$

where $i_{corr}$ is the corrosion current density; $\beta_c$ is the cathodic Tafel slope, and $\beta_a$ is the anodic Tafel slope. Eventually, the calculations of the output results were based on the polarization curves for Ni–Ti SMAs.

## Results and Discussion

### Microstructure Characterization

The elevation in the temperature had a profound effect on the diffusion of Ni, as evident in Fig. 2a–d. It can be observed that all the previous parameters failed to satisfy the main purpose of the PM to produce near-net component without requiring machining and finishing. The diffusion of titanium atoms into nickel is slower than that of nickel atoms into titanium [42, 43], and hence pore formation in the Ni-rich region was caused by an imbalance of mass transfer. The diffusion rate increased with sintering temperature, and more pores were formed [42, 43]. The porosity ratio is time- and temperature-dependent. The pore size and pore distribution of the Ni–Ti sample fabricated by microwave sintering are similar to the conventional sintering process. Both time and temperature primarily affect the resulting pore characteristics [42, 44]. For this reason, it is recommended that one reduces the temperature to avoid or adjust the diffusion of the nickel at a certain time point. Figure 2d shows a cross section of a partially melted 51%Ni–Ti sample. The spherical pores near the surface of the sample were created by trapped gas and formed during out gassing from the sample due to the short sintering duration. Figure 2e shows a uniform outer surface of a Ni–Ti sample sintered at 700 °C for 15 min. Figure 2f shows the optical micrographs of Ni–Ti samples, whereas both samples have small pores with the size in the range of 3–50 μm and an average pore size of ∼ 7 μm for (a) and ∼ 9 μm for (b). The macro-sized pores that formed via the microwave sintering process may facilitate bone tissue growth and integrate with the surrounded bone [25–27, 45]. Table 2 lists the effect of sintering parameters on relative density.

The micrographs of microwave-sintered 51%Ni–Ti samples presented in Fig. 3 show the microstructure of two sintering temperatures at a sintering time of 15 min. EDS shows Ti-rich and Ni-rich regions with $Ti_2Ni$, NiTi, and $Ni_3Ti$ phases between the two. The diffusion of Ni towards Ti occurs from Ni → $Ni_3Ti$ → NiTi → $Ti_2Ni$ → Ti, and the reverse occurs for Ti [46]. From the Ni–Ti phase diagram, β-Ti and $Ti_2Ni$ intermetallics should be in contact within the microstructure [16]. A plate-like structure morphology appeared for sample sintered at 700 °C (located in Ti-rich region) clearly after etching with 10%HF–40%$HNO_3$–50% distilled water solution for 15–30 s, but the plates-like structure morphology did not appeared in Ti-rich region for the sample sintered at 550 °C. The

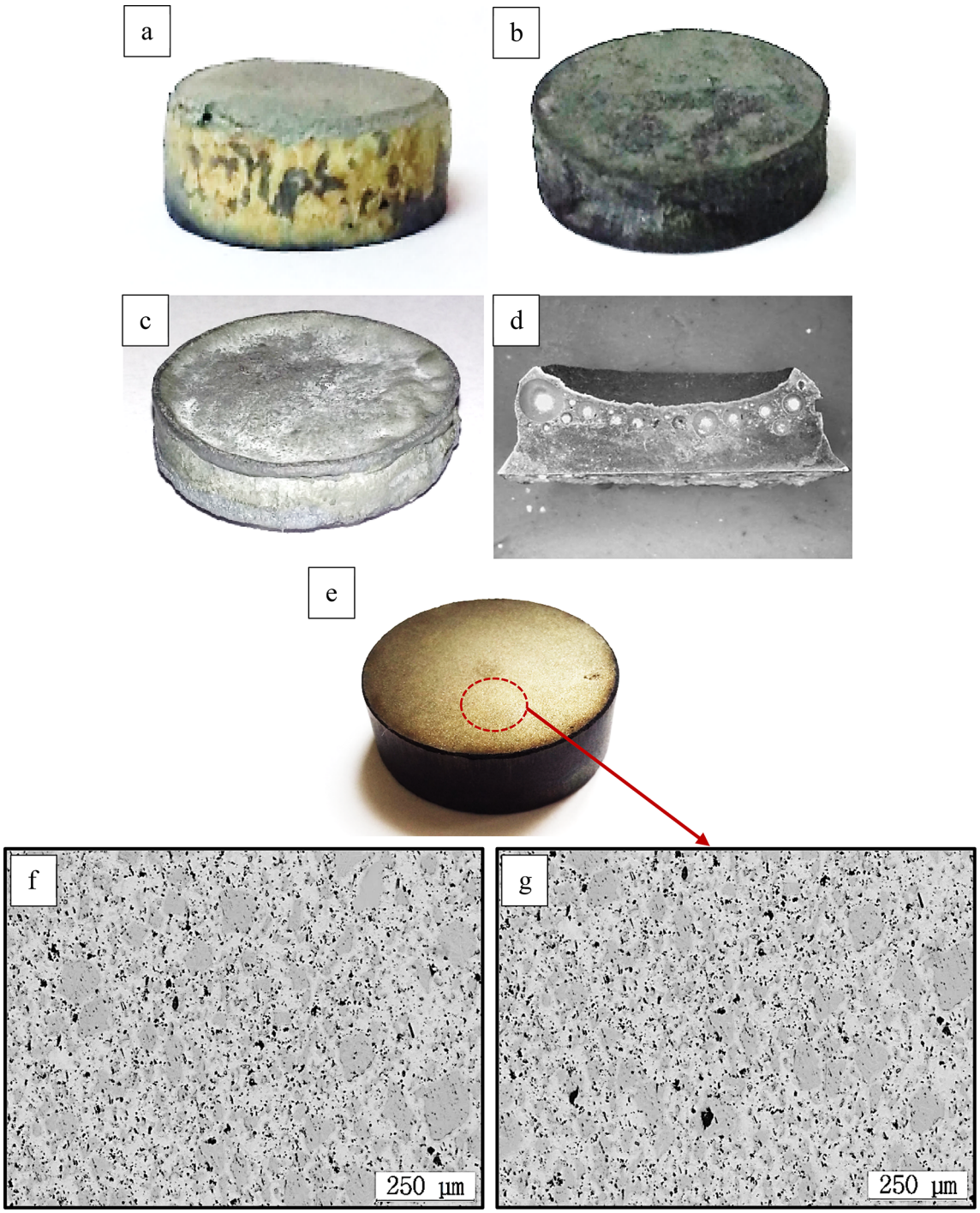


**Fig. 2** **a** Swelling of the sample sintered at 800 °C for 5 min, **b** non-uniform shrinkage of the sintered sample at 800 °C for 30 min, **c** sample sintered at 900 °C for 30 min, **d** cross section of partially melted 51%Ni–Ti sample after MWS at a temperature of 1200 °C for 5 min and **e** sample sintered at 700 °C for 15 min. **f** Optical micrographs of sample sintered at 550 °C for 15 min and **g** optical micrograph of sample sintered at 700 °C for 15 min

**Table 2** Effect of sintering parameters on relative density of the 51%Ni–Ti alloy

| Sintering parameters | Temperature (°C): | 550 | 700 | 800 | 800 | 900 | 900 | 1000 | 1000 |
|---|---|---|---|---|---|---|---|---|---|
| | Time (min): | 15 | 15 | 5 | 30 | 5 | 30 | 5 | 30 |
| Relative density ($\rho/\rho_0$) % | 79 | 80 | 71 | 78 | 83.5 | 87 | 80 | 79.8 | |

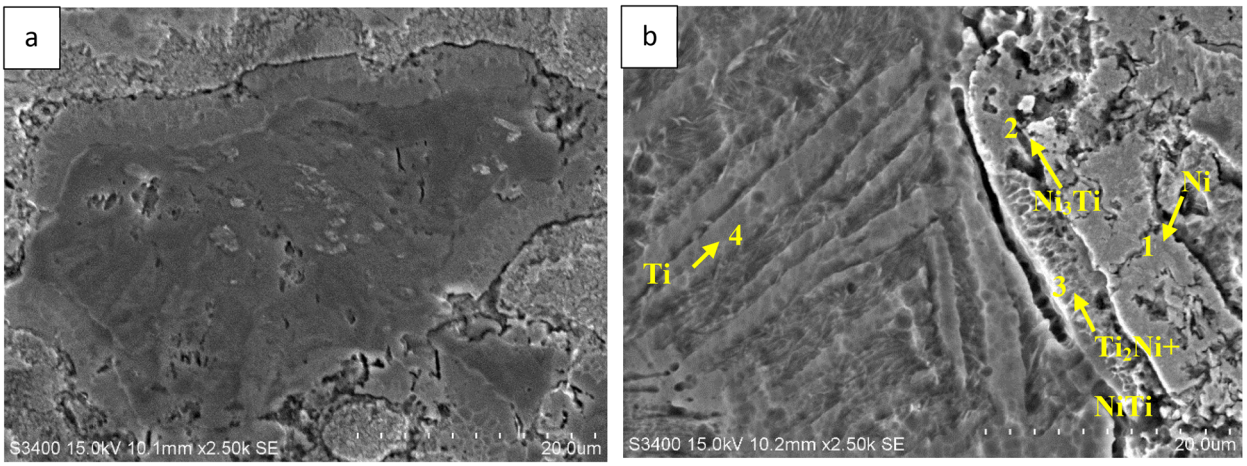


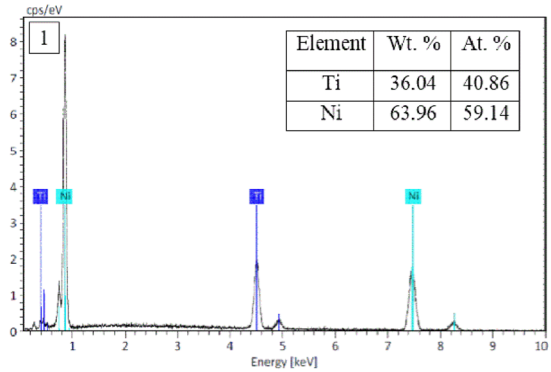


| Element | Wt. % | At. % |
|---|---|---|
| Ti | 36.04 | 40.86 |
| Ni | 63.96 | 59.14 |

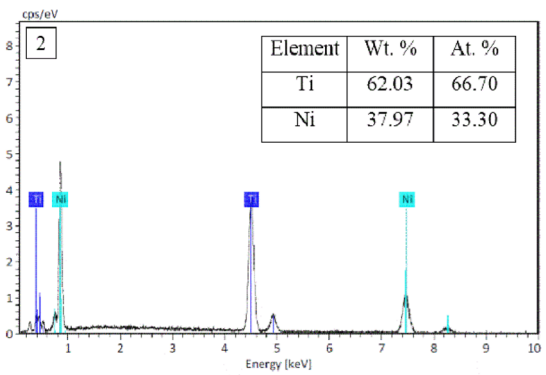


| Element | Wt. % | At. % |
|---|---|---|
| Ti | 62.03 | 66.70 |
| Ni | 37.97 | 33.30 |

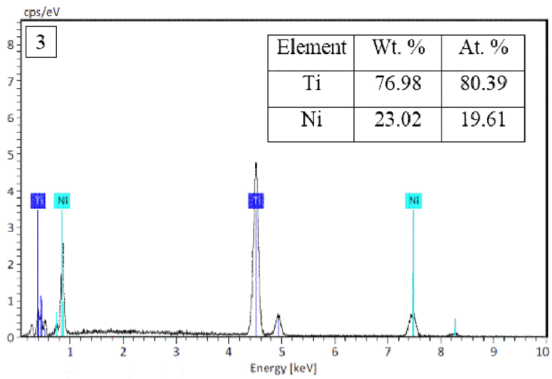


| Element | Wt. % | At. % |
|---|---|---|
| Ti | 76.98 | 80.39 |
| Ni | 23.02 | 19.61 |

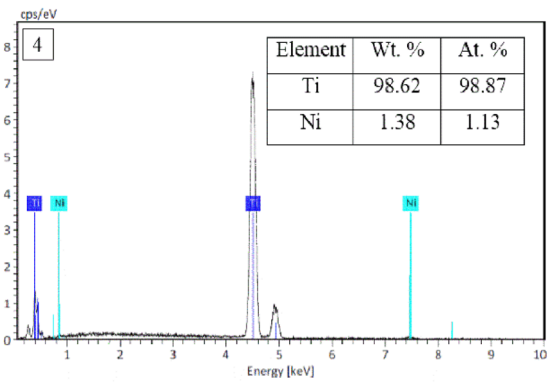


| Element | Wt. % | At. % |
|---|---|---|
| Ti | 98.62 | 98.87 |
| Ni | 1.38 | 1.13 |

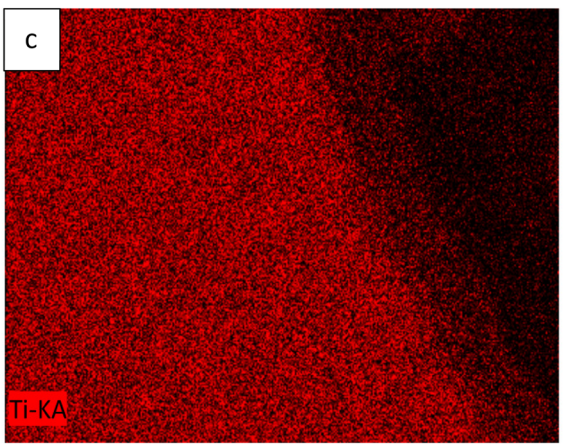


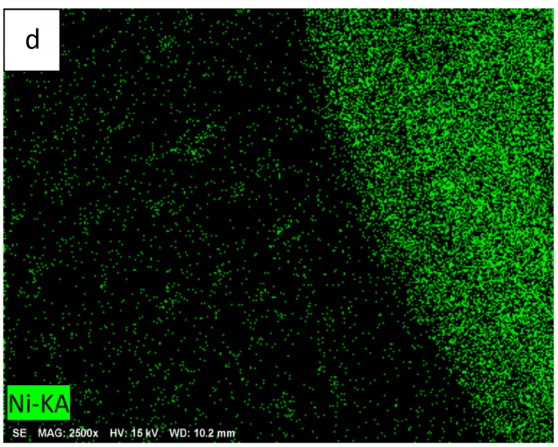

◀**Fig. 3** SEM micrographs of Ni–Ti samples sintered at temperatures and times: **a** 550 °C for 15 min, **b** Sintering at 700 °C for 15 min with EDS analysis at spots 1, 2, 3, and 4: and **c**, **d** elemental mapping of sintered 51%Ni–Ti SMA at 700 °C for 15 min

density of these two samples was 79 and 80%, and the porosity was 21 and 20% for the samples sintered at 550 and 700 °C, respectively. The plates disappeared with a decrease in the sintering temperature to 550 °C. Figure 3b depicts the EDS spot results of the sample sintered at 700 °C for 15 min. There were two specific regions, beginning with the Ni-rich region moving toward the Ti-rich region and between them are the $Ti_2Ni$, NiTi, and $Ni_3Ti$ phase. The elemental mapping of Ti and Ni from the micrograph survey in Fig. 2b is shown in Fig. 3c, d. Ti and Ni, along with regions which appears to contain $Ti_2Ni$, NiTi, and $Ni_3Ti$ phases between the Ti- and Ni-rich regions, were observed.

Figure 4 depicts the XRD patterns of MWS 51%Ni–Ti SMAs with varying sintering parameters. The alloy phases formed were B2 (NiTi), B19′ (NiTi), $Ni_3Ti$, and $Ti_2Ni$. The presence of the secondary phases of $Ni_3Ti$ and $Ti_2Ni$ was due to the solid-state diffusion reaction. The existence of the TiNi phase was based on the primary reaction between Ti and Ni, while the formation of the secondary phases, $Ni_3Ti$ and $Ti_2Ni$, stemmed from incomplete reactions based on Ni–Ti forming through the thermodynamically weak reactions between $Ni_3Ti$ and $Ti_2Ni$ [20, 47]. Figure 4 also portrays the XRD patterns of MWS Ni–Ti at two different sintering temperatures showing the B2 (Ni–Ti), B19′ (Ni–Ti), $Ni_3Ti$, and $Ti_2Ni$ phases [48]. There was also evidence of the R-phase and $TiO_2$. The XRD results did not show the $Ni_4Ti_3$ precipitates because these precipitates mainly

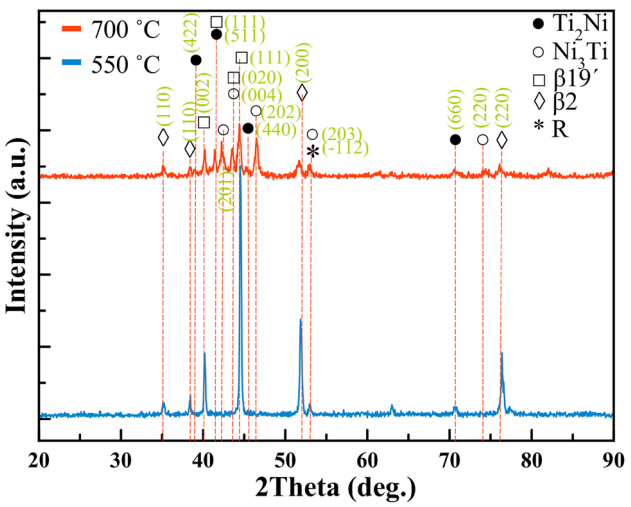


**Fig. 4** XRD pattern of 51%Ni–Ti MWS samples sintered at 550 and 700 °C for 15 min

appear due to aging process which was not performed in this work [49–51]. It was reported in the literature that the production of 51(at.%)Ni–Ti alloys via microwave sintering process without aging confirms the presence of the B2 (TiNi), B19′ (TiNi), $Ni_3Ti$, and $Ti_2Ni$ phases without the $Ni_4Ti_3$ precipitates [19, 20]. Bassani et al. [52] reported that $Ti_2Ni$ revealed a biocompatibility close to or even better than NiTi; therefore, it is possibly that the presence of the $Ti_2Ni$ phase does not affect the biocompatibility of the MWS NiTi material. The presence of $Ni_3Ti$ was characterized by a substantial higher nickel release rate. Further tests on the MWS Ni–Ti material with different topography and/or secondary phase contents could further elucidate the observed phenomena [52].

## Differential Scanning Calorimeter (DSC) of 51%Ni–Ti SMAs

Figure 5 displays the DSC curves of the 51%Ni–Ti samples. A multi-step phase transformation was observed from B19′ to B2 (B19′ → R → B2) during heating on the sample sintered at 700 °C. The presence of the R-phase during heating of Ni–Ti SMAs was also reported by other researchers [53]. During cooling, it followed the same multi-step phase transformation from B2 to B19′ (B2 → R → B19′). Table 3 gives the transformation temperature of the 51%Ni–Ti SMA sintered at 700 °C. The table presents only the 700 °C data, because the peaks were too weak to interpret for the 550 °C sample.

## Compressive Test of 51%Ni–Ti SMAs

Figure 6 shows the compressive strength curves of the 51%Ni–Ti samples. The initial stage was marked with a low slope in the compressive curves for the samples which were sintered at 550 °C. By ignoring this initial stage, the compressive curves in Fig. 6 can be divided into three regions [54]. The first region is based on a linear elastic deformation where the slope considers the elastic modulus of the samples. The second region is a plastic yield deformation region in which peak stress observed and is considered as the compressive strength of the samples. Lastly, the third region is the failure region in which sample fracture occurred. The highest maximum stress and strain were for the samples sintered at 700 °C. Table 4 lists the maximum strength and its strain, elastic modulus and Vickers hardness of Ni–Ti samples sintered at 700 and 550 °C for 15 min. The difference in the compressive strength and strain between these two alloys may be due to the low temperature (550 °C) which may be insufficient for a complete bonding to take place. The Vickers hardness was low for sample sintered at 550 °C comparing with the sample sintered at 700 °C. The low Vickers hardness of

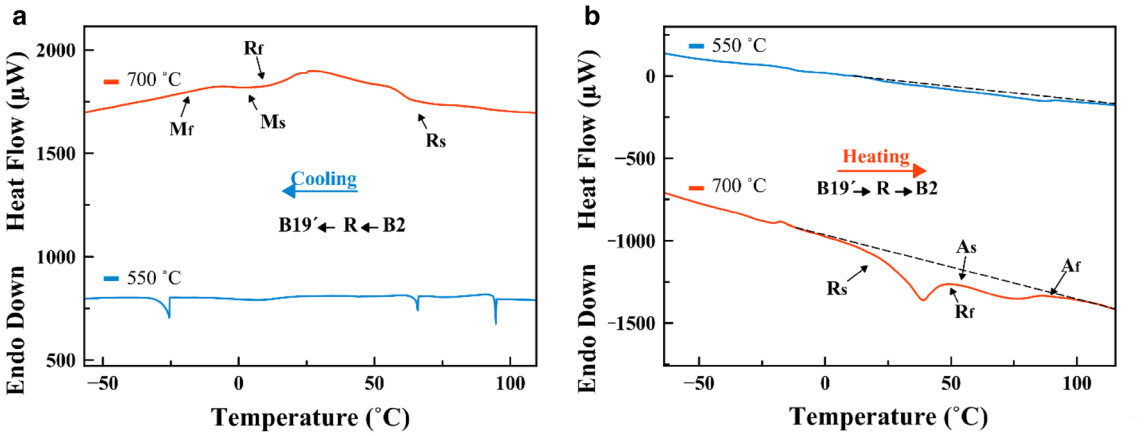


**Fig. 5** Differential scanning calorimeter (DSC) curves of 51%Ni–Ti samples microwave sintered at different temperatures for 15 min **a** during cooling and **b** during heating

**Table 3** Ni–Ti transformation temperatures

| Ti–Ni alloys parameters | $R_s$ (°C) cooling | $R_f$ (°C) cooling | $M_s$ (°C) | $M_f$ (°C) | $R_s$ (°C) heating | $R_f$ (°C) heating | $A_s$ (°C) | $A_f$ (°C) |
|---|---|---|---|---|---|---|---|---|
| Ti–Ni (700 °C) | 63 | 9 | 3 | − 18 | 21 | 48 | 54 | 89 |

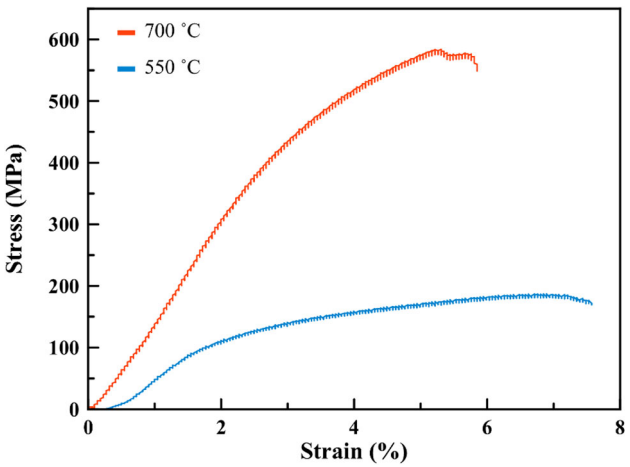


**Fig. 6** Compressive stress–strain curves of Ni–Ti samples with two different microwave sintering temperatures for 15 min

in biomedical devices [19, 55]. The fabrication of alloys with low elastic modulus is important to solve the problem of "stress shielding" [28–30]. The compression stress and strain normally depend on several properties such as density, pore size, pore shape, pore distribution, grain size, structure, precipitate formations, and degree of order.

## Bio-corrosion Test

Figure 7 shows the electrochemical polarization curve of the Ni–Ti SMA sintered at 700 and 550 °C in SBF solution, which depicts, the corrosion potential and the current density. For the sample sintered at 700 °C, the corrosion potential ($E_{corr}$) of the Ni–Ti SMA was − 65.359 mV; the current density ($i_{corr}$) was 32.17 μA/cm$^2$; the cathodic slope ($\beta_c$) was 207.099 mV, while the anodic slope ($\beta_a$) was

**Table 4** Effect of sintering parameters on relative strength, strain, and elastic modulus

| Ti–Ni alloy parameters | Maximum strength (MPa) | Strain at maximum strength (%) | Elastic modulus (GPa) | Vickers hardness (HV) |
|---|---|---|---|---|
| 550 °C and 15 min | 187 | 6.89 | 7.8 | 73.9 |
| 700 °C and 15 min | 581 | 5.26 | 14.28 | 152 |

these samples maybe attributed to the microwave sintering method, as well as the low elastic modulus, the presence of porosity and low elastic modulus may affect the application

358.538 mV; the polarization resistance ($R_p$) was 1.774 kΩ; and corrosion rate ($R_i$) was 0.73508 mm/year. The key limitation of using Ni–Ti for medical implants,

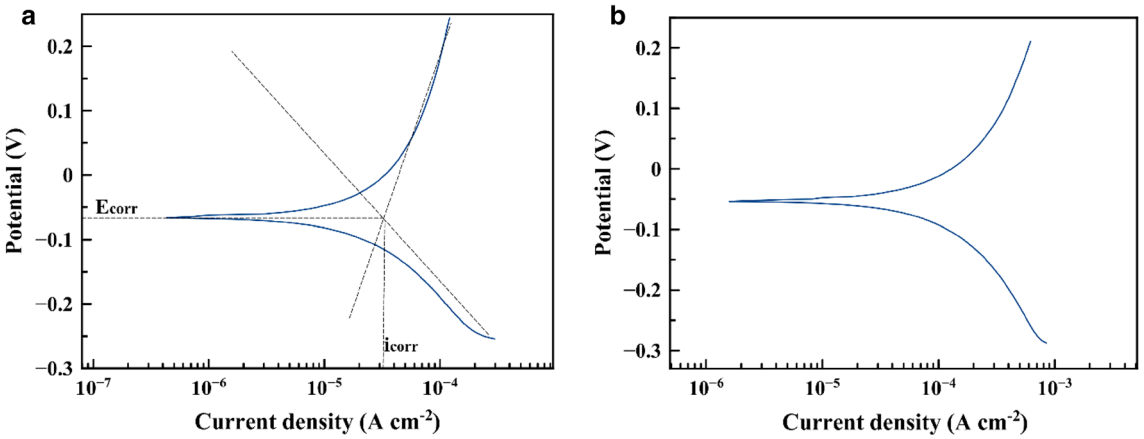


**Fig. 7** Electrochemical polarization curves of Ni–Ti in the simulated body fluid (SBF), **a** the simple sintered at 700 °C with indicated $E_{corr}$ and $i_{corr}$ and **b** sample sintered at 550 °C

according to the literature, is the moderate cell culture compatibility and corrosion resistance [56]. The sample sintered at 550 °C exhibited the following values: corrosion potential ($E_{corr}$) of − 53.372 mV, current density ($i_{corr}$) of 171.26 μA/cm$^2$, cathodic slope ($\beta_c$) of 298 mV, anodic slope ($\beta_a$) of 352 mV, polarization resistance ($R_p$) of 0.409 kΩ, and corrosion rate ($R_i$) of 3.913 mm/year. A decrease in the sintering temperature from 700 to 550 °C severely deteriorates the corrosion resistance of 51%Ni–Ti SMAs.

## Conclusions

The experimental results can be summarized:

1. The microstructure shows two main regions (Ti-rich and Ni-rich regions), between the Ti region and Ni region appear $Ti_2Ni$, NiTi, and $TiNi_3$ phases. The microstructure shows plates-like morphology located in Ti-rich region for sample sintered at 700 °C and this plates-like morphology was not present for sample sintered at 550 °C.
2. XRD-patterns show B2 (NiTi), B19′ (NiTi), $Ni_3Ti$, and $Ti_2Ni$ phases. There is also an evidence of the R-phase and $TiO_2$.
3. DSC curves display during cooling, a multi-step phase transformation from B2 to R and R, to B19′ and the reverse during heating. The $M_s$, $A_s$, and $A_f$ temperatures were more than 0 °C.
4. The highest fracture strength and its strain, as well as the spring back strain and the lowest corrosion rate were found when sintering at 700 °C, relative to the samples sintered at 550 °C. The use of MWS Ni–Ti with a low elastic modulus could potentially eliminate the effect of "stress shielding" substantiating the use of the material in the biomedical applications.

**Acknowledgements** The authors would like to thank the Ministry of Higher Education of Malaysia and Universiti Teknologi Malaysia for providing the financial support under the University Research Grant No. Q.J130000.2524.12H60 and research facilities.

## References

1. Liu Y (2015) The superelastic anisotropy in a NiTi shape memory alloy thin sheet. Acta Mater 95:411–427
2. Long M, Rack H (1998) Titanium alloys in total joint replacement—a materials science perspective. Biomaterials 19(18):1621–1639
3. Huiskes R, Weinans H, Van Rietbergen B (1992) The relationship between stress shielding and bone resorption around total hip stems and the effects of flexible materials. Clin Orthop Relat Res 274:124–134
4. Wever D, Veldhuizen A, De Vries J, Busscher H, Uges D, Van Horn J (1998) Electrochemical and surface characterization of a nickel–titanium alloy. Biomaterials 19(7):761–769
5. Plant SD, Grant DM, Leach L (2005) Behaviour of human endothelial cells on surface modified NiTi alloy. Biomaterials 26(26):5359–5367
6. Mockers O, Deroze D, Camps J (2002) Cytotoxicity of orthodontic bands, brackets and archwires in vitro. Dent Mater 18(4):311–317
7. Ryhänen J, Kallioinen M, Tuukkanen J, Junila J, Niemelä E, Sandvik P, Serlo W (1998) In vivo biocompatibility evaluation of nickel-titanium shape memory metal alloy: muscle and perineural tissue responses and encapsule membrane thickness. J Biomed Mater Res 41(3):481–488
8. Itin V, Gyunter V, Shabalovskaya S, Sachdeva R (1994) Mechanical properties and shape memory of porous nitinol. Mater Charact 32(3):179–187
9. Tang SM, Chung CY, Liu WG (1997) Preparation of Cu-AI-Ni-based shape memory alloys by mechanical alloying and powder metallurgy method. J Mater Process Technol 63:307–312
10. Ibarra A, Juan JS, Bocanegra EH, Nó ML (2006) Thermo-mechanical characterization of Cu–Al–Ni shape memory alloys

elaborated by powder metallurgy. Mater Sci Eng A 438–440:782–786
11. Zhao Y, Taya M, Kang Y, Kawasaki A (2005) Compression behavior of porous NiTi shape memory alloy. Acta Mater 53(2):337–343
12. Wu S, Liu X, Chu P, Chung C, Chu C, Yeung K (2008) Phase transformation behavior of porous NiTi alloys fabricated by capsule-free hot isostatic pressing. J Alloys Compd 449(1):139–143
13. Bertheville B, Neudenberger M, Bidaux J-E (2004) Powder sintering and shape-memory behaviour of NiTi compacts synthesized from Ni and $TiH_2$. Mater Sci Eng A 384(1):143–150
14. Li B-Y, Rong L-J, Li Y-Y (1998) Porous NiTi alloy prepared from elemental powder sintering. J Mater Res 13(10):2847–2851
15. Zanotti C, Giuliani P, Terrosu A, Gennari S, Maglia F (2007) Porous Ni–Ti ignition and combustion synthesis. Intermetallics 15(3):404–412
16. Li B-Y, Rong L-J, Li Y-Y, Gjunter V (2000) A recent development in producing porous Ni–Ti shape memory alloys. Intermetallics 8(8):881–884
17. Aust E, Limberg W, Gerling R, Oger B, Ebel T (2006) Advanced TiAl6Nb7 bone screw implant fabricated by metal injection moulding. Adv Eng Mater 8(5):365–370
18. Benson J, Chikwanda H (2009) The challenges of titanium metal injection moulding. J New Gener Sci 7(3):1–14
19. Xu J, Bao L, Liu A, Jin X, Tong Y, Luo J, Zhong Z, Zheng Y (2015) Microstructure, mechanical properties and superelasticity of biomedical porous NiTi alloy prepared by microwave sintering. Mater Sci Eng C 46:387–393
20. Tang C, Zhang L, Wong C, Chan K, Yue T (2011) Fabrication and characteristics of porous NiTi shape memory alloy synthesized by microwave sintering. Mater Sci Eng A 528(18):6006–6011
21. Oghbaei M, Mirzaee O (2010) Microwave versus conventional sintering: a review of fundamentals, advantages and applications. J Alloys Compd 494(1–2):175–189
22. Das S, Mukhopadhyay A, Datta S, Basu D (2009) Prospects of microwave processing: an overview. Bull Mater Sci 32(1):1–13
23. Roy R, Agrawal D, Cheng J, Gedevanishvili S (1999) Full sintering of powdered-metal bodies in a microwave field. Nature 399(6737):668–670
24. Yang D, Guo Z, Shao H, Liu X, Ji Y (2012) Mechanical properties of porous Ti-Mo and Ti-Nb alloys for biomedical application by gelcasting. Procedia Eng 36:160–167
25. Mour M, Das D, Winkler T, Hoenig E, Mielke G, Morlock MM, Schilling AF (2010) Advances in porous biomaterials for dental and orthopaedic applications. Materials 3(5):2947–2974
26. Bansiddhi A, Sargeant T, Stupp SI, Dunand D (2008) Porous NiTi for bone implants: a review. Acta Biomater 4(4):773–782
27. Ryan G, Pandit A, Apatsidis DP (2006) Fabrication methods of porous metals for use in orthopaedic applications. Biomaterials 27(13):2651–2670
28. Geetha M, Singh A, Asokamani R, Gogia A (2009) Ti based biomaterials, the ultimate choice for orthopaedic implants—a review. Prog Mater Sci 54(3):397–425
29. Nagels J, Stokdijk M, Rozing PM (2003) Stress shielding and bone resorption in shoulder arthroplasty. J Shoulder Elbow Surg 12(1):35–39
30. Niinomi M (2008) Metallic biomaterials. J Artif Organs 11(3):105–110
31. Nouri A (2008) Novel metal structures through powder metallurgy for biomedical applications
32. Nouri A, Hodgson PD, Wen CE (2010) Biomimetic porous titanium scaffolds for orthopaedic and dental applications. InTech, Croatia
33. Özgen C (2007) Production and characterization of porous titanium alloys. Middle East Technical University, Ankara
34. Wen C, Mabuchi M, Yamada Y, Shimojima K, Chino Y, Asahina T (2001) Processing of biocompatible porous Ti and Mg. Scr Mater 45(10):1147–1153
35. Bram M, Stiller C, Buchkremer HP, Stöver D, Baur H (2000) High-porosity titanium, stainless steel, and superalloy parts. Adv Eng Mater 2(4):196–199
36. Wen CE, Yamada Y, Nouri A, Hodgson PD (2007) Porous titanium with porosity gradients for biomedical applications, materials science forum. Trans Tech Publication, Zürich, pp 720–725
37. Dewidar MM, Lim J (2008) Properties of solid core and porous surface Ti–6Al–4V implants manufactured by powder metallurgy. J Alloys Compd 454(1):442–446
38. Zhang Y, Li D, Zhang X (2007) Gradient porosity and large pore size NiTi shape memory alloys. Scr Mater 57(11):1020–1023
39. Rausch G, Banhart J (2002) Making cellular metals from metals other than aluminum. Handbook of cellular metals. Wiley-VCH, Weinheim, pp 21–28
40. Bakhsheshi-Rad H, Idris M, Abdul-Kadir M, Ourdjini A, Medraj M, Daroonparvar M, Hamzah E (2014) Mechanical and biocorrosion properties of quaternary Mg–Ca–Mn–Zn alloys compared with binary Mg–Ca alloys. Mater Des 53:283–292
41. Argade G, Kandasamy K, Panigrahi S, Mishra R (2012) Corrosion behavior of a friction stir processed rare-earth added magnesium alloy. Corros Sci 58:321–326
42. Zhu S, Yang X, Hu F, Deng S, Cui Z (2004) Processing of porous TiNi shape memory alloy from elemental powders by Ar-sintering. Mater Lett 58(19):2369–2373
43. Sadrnezhaad SK, Lashkari O (2006) Property change during fixtured sintering of NiTi memory alloy. Mater Manuf Process 21(1):87–96
44. Hey J, Jardine A (1994) Shape memory TiNi synthesis from elemental powders. Mater Sci Eng A 188(1):291–300
45. Akin FA, Zreiqat H, Jordan S, Wijesundara MB, Hanley L (2001) Preparation and analysis of macroporous $TiO_2$ films on Ti surfaces for bone–tissue implants. J Biomed Mater Res 57(4):588–596
46. Locci A, Orru R, Cao G, Munir ZA (2003) Field-activated pressure-assisted synthesis of NiTi. Intermetallics 11(6):555–571
47. Laeng J, Xiu Z, Xu X, Sun X, Ru H, Liu Y (2007) Phase formation of Ni–Ti via solid state reaction. Phys Scr 2007(T129):250
48. Liu A, Gao Z, Gao L, Cai W, Wu Y (2007) Effect of Dy addition on the microstructure and martensitic transformation of a Ni-rich TiNi shape memory alloy. J Alloys Compd 437(1):339–343
49. Khalil-Allafi J, Dlouhy A, Eggeler G (2002) $Ni_4Ti_3$-precipitation during aging of NiTi shape memory alloys and its influence on martensitic phase transformations. Acta Mater 50(17):4255–4274
50. El-Bagoury N (2015) Precipitation of second phases in aged Ni rich NiTiRe shape memory alloy. Mater High Temp 32(4):390–398
51. Hastuti K, Hamzah E, Hashim J (2014) Effect of ageing temperatures on the transformation behaviour of Ti-507 at% Ni shape memory alloy. Advanced materials research. Trans Tech Publication, Zürich, pp 108–112
52. Bassani P, Panseri S, Ruffini A, Montesi M, Ghetti M, Zanotti C, Tampieri A, Tuissi A (2014) Porous NiTi shape memory alloys produced by SHS: microstructure and biocompatibility in comparison with Ti2Ni and TiNi3. J Mater Sci Mater Med 25(10):2277–2285
53. Su P, Wu S (2004) The four-step multiple stage transformation in deformed and annealed Ti49Ni51 shape memory alloy. Acta Mater 52(5):1117–1122

54. Gao Z, Li Q, He F, Huang Y, Wan Y (2012) Mechanical modulation and bioactive surface modification of porous Ti–10Mo alloy for bone implants. Mater Des 42:13–20
55. Xu J, Bao L, Liu A, Jin X, Luo J, Zhong Z, Zheng Y (2015) Effect of pore sizes on the microstructure and properties of the biomedical porous NiTi alloys prepared by microwave sintering. J Alloys Compd 645:137–142
56. Fraker A, Ruff A, Sung P, Van Orden A, Speck K (1983) Surface preparation and corrosion behavior of titanium alloys for surgical implants. Titanium alloys in surgical implantsed. ASTM International, West Conshohocken